Monopole transitions to cluster states in [10]Be and [9]Li

AUTHOR(S):

Kanada-En'Yo, Yoshiko

CITATION:

Kanada-En'Yo, Yoshiko. Monopole transitions to cluster states in [10]Be and [9]Li. Physical Review C - Nuclear Physics 2016, 94(2): 024326.

ISSUE DATE:

2016-08-18

URL:

http://hdl.handle.net/2433/218374

PHYSICAL REVIEW C **94**, 024326 (2016)

Monopole transitions to cluster states in ^{10}Be and ^{9}Li

Yoshiko Kanada-En'yo
Department of Physics, Kyoto University, Kyoto 606-8502, Japan
(Received 7 April 2016; revised manuscript received 3 June 2016; published 18 August 2016)

Isoscalar monopole transitions from the ground states to cluster states in ^{10}Be and ^{9}Li are investigated using ^{6}He + α and ^{6}He + t cluster models, respectively. In ^{10}Be, significant monopole strengths are obtained for ^{6}He + α cluster resonances of ^{10}Be($0^+_{3,4}$) above the α-decay threshold, whereas the strengths for ^{6}He + t cluster resonances in ^{9}Li are not enhanced because of the large fragmentation of strengths in the corresponding energy region. The monopole transition to ^{10}Be(0^+_2) with the molecular orbital structure is relatively weak compared with those to ^{6}He + α cluster resonances. Monopole strength distributions do not directly correspond to distributions of ^{6}He(0^+) + α and ^{6}He(0^+) + t components but reflect the component of the deformed ^{6}He cluster with a specific orientation, which is originally embedded in the ground state.

DOI: 10.1103/PhysRevC.94.024326

I. INTRODUCTION

Recently, various exotic cluster states have been discovered in neutron-rich nuclei. Neutron-rich Be isotopes are typical examples in which various cluster structures appear in the ground and excited states (for example, Refs. [1–4] and references therein). Low-lying states in Be isotopes can be understood based on a molecular orbital picture in which valence neutrons in molecular orbitals around a 2α core are considered [1,3–28]. In highly excited states above the He+He threshold energy, dinuclear-type He+He resonances (cluster resonances) are expected to appear as suggested by the cases of ^{10}Be and ^{12}Be [1,3,4,17,19–49].

The coexistence of molecular orbital structures and cluster resonances in ^{12}Be has been intensively studied experimentally and theoretically. The ground state of ^{12}Be is a largely deformed intruder state, in which two neutrons occupy a longitudinal molecular orbital—the so-called the σ orbital—around the 2α core. Highly excited states observed in ^{6}He + ^{6}He and ^{8}He + ^{4}He decays above the threshold energies are regarded to be cluster resonances [46–49]. In theoretical studies using the generalized two-center cluster model (GTCM), Ito *et al.* predicted that ^{8}He + ^{4}He, ^{6}He + ^{6}He, and ^{7}He + ^{5}He cluster resonances appear in the energy region a few MeV above the threshold energies [4,24,26,27]. They discussed monopole transitions from the ground state to the excited states and showed that the monopole strength for the ^{8}He + ^{4}He cluster resonance is strongly enhanced, which suggests that monopole excitations can be a good probe to experimentally observe cluster resonances.

The coexistence of molecular orbital structures and cluster resonances has also been investigated for ^{10}Be. Theoretical works have predicted that the $K^\pi = 0^+_2$ band is constructed by a largely deformed state featuring a molecular orbital structure with two σ-orbital neutrons around the developed 2α core. In the experimental energy levels, the 0^+_2 state at 6.18 MeV, 2^+ state at 7.54 MeV, and 4^+ state at 10.2 MeV are assigned to the $K^\pi = 0^+_2$ band [32,34,38,39], although the spin and parity of the 10.2 MeV state have not yet been established [36]. Above the $K^\pi = 0^+_2$ band, ^{6}He + α cluster resonances have been theoretically predicted [4,50]; however, there is as yet no experimental evidence of a cluster resonance state above the ^{6}He + α decay threshold in ^{10}Be. A state observed in inelastic ^{6}He + α scattering is a candidate for a ^{6}He(2^+) + α resonance state [42]. There is also an experimental report on a broad resonance in ^{10}B, which is regarded as the mirror state of a ^{6}He + α cluster resonance [51].

In analogy to ^{10}Be, cluster states in excited states of ^{9}Li have been theoretically studied using a ^{6}He + t cluster model by the author and her collaborators [52]. They predicted ^{6}He(0^+) + t cluster resonances in highly excited states above the t-decay threshold, which can be analogous to ^{6}He(0^+) + α cluster resonances in ^{10}Be. It was also shown that molecular orbital structures do not appear in ^{9}Li because molecular orbitals are unfavored around the asymmetric core of $\alpha + t$, in contrast to the symmetric core of 2α in ^{10}Be.

In this paper, I investigate monopole excitations from the ground state to the excited ^{10}Be(0^+) and ^{9}Li($3/2^-$) states. I focus on the monopole strengths of cluster resonances in order to determine whether monopole strengths can be probes for observing cluster resonances. To this end, I adopt the generator coordinate method (GCM) [53] of the ^{6}He + α and ^{6}He + t cluster models, which was used to investigate cluster states in ^{9}Li and ^{10}Be in a previous work [52]. I reanalyze ^{9}Li($3/2^-$) and ^{10}Be(0^+) states while focusing on monopole excitations. This method has been shown to well describe experimental properties of the ground and the second 0^+ bands in ^{10}Be. In the calculation, resonance states are obtained in a bound-state approximation. I estimate the cluster decay widths of cluster resonances by approximating the reduced width amplitudes at channel radii and by changing the size of the box boundary. The monopole strengths for transitions from the ground state to the excited states are also investigated. Cluster components in the ground and excited states are calculated, and their relation to monopole excitations is discussed.

The rest of the paper is organized as follows. In Sec. II, I explain the formulation of the present calculation. I show the calculated results in Sec. III and discuss cluster structures and monopole excitations in Sec. IV. Finally, a summary and an outlook are given in Sec. V.

II. FORMULATION

A. ^{6}He + $\alpha(t)$ cluster wave functions

As was done in the previous work [52], the Bloch-Brink wave functions [54] of ^{6}He + α and ^{6}He + t cluster wave functions are used here. The ^{6}He and $\alpha(t)$ cluster wave functions are written using harmonic oscillator (ho) shell-model wave functions localized at $\boldsymbol{S}_1 = (0,0,-\frac{A_2}{A}D)$ and $\boldsymbol{S}_2 = (0,0,+\frac{A_1}{A}D)$, respectively. Here A_1 and A_2 are the mass numbers of two clusters and A is the total mass number $A = A_1 + A_2$. D indicates the distance parameter, which is treated as the generator coordinate in the superposition of basis wave functions. A common width parameter $\nu = 1/2b^2 = 0.235$ fm^{-2} is used for ^{6}He, α, and t clusters.

The α and t clusters are expressed by the $(0s)^2_\pi(0s)^2_\nu$ and $(0s)_\pi(0s)^2_\nu$ configurations, respectively. For the ^{6}He cluster, the p-shell configurations of two valence neutrons around an α cluster, $(0s)^2_\pi(0s)^2_\nu(0p)^2_\nu$, are used. To express p-shell configurations, I use the hybrid model space of basis wave functions combining ls and jj coupling schemes as was done in the previous work. For the configurations favored in the ls coupling scheme, $|p_z,n\uparrow\rangle|p_z,n\downarrow\rangle$ and its rotated configurations are used to take into account ^{6}He$(0^+,2^+)$ states with the two-neutron intrinsic spin $S_{12} = 0$. For configurations favored in the jj coupling scheme, $|p_{(+)},n\uparrow\rangle|p_{(-)},n\downarrow\rangle$ and its rotated configurations are adopted to take into account ^{6}He$(0^+,2^+)$ states in the $p^2_{3/2}$ configurations. Here, $p_{(+)},p_z,p_{(-)}$ stand for the ho p orbits with $l_z = +1,0,-1$, respectively (l_z is the z component of the orbital angular momentum $\boldsymbol{l}$). Note that the hybrid model space of these ls coupling and jj coupling configurations for the ^{6}He cluster is equivalent to the full model space of p-shell configurations for ^{6}He$(0^+,2^+)$.

The ^{6}He + α and ^{6}He + t cluster wave functions projected onto parity and total-angular-momentum eigenstates are written as

$$\begin{aligned} P^{J\pi}_{MK}|\Phi_\tau(D)\rangle = P^{J\pi}_{MK}\mathcal{A}\{&|\psi_{1\tau}(\boldsymbol{S}_1)\rangle|\psi_{2\tau}(\boldsymbol{S}_1)\rangle \\ &\times|\phi(\boldsymbol{S}_1)p\uparrow\rangle|\phi(\boldsymbol{S}_1)p\downarrow\rangle|\phi(\boldsymbol{S}_1)n\uparrow\rangle|\phi(\boldsymbol{S}_1)n\downarrow\rangle \\ &\times|\phi(\boldsymbol{S}_2)p\uparrow\rangle|\phi(\boldsymbol{S}_2)p\downarrow\rangle|\phi(\boldsymbol{S}_2)n\uparrow\rangle|\phi(\boldsymbol{S}_2)n\downarrow\rangle\} \end{aligned} \tag{1}$$

and

$$\begin{aligned} P^{J\pi}_{MK}|\Phi_\tau(D)\rangle = P^{J\pi}_{MK}\mathcal{A}\{&|\psi_{1\tau}(\boldsymbol{S}_1)\rangle|\psi_{2\tau}(\boldsymbol{S}_1)\rangle \\ &\times|\phi(\boldsymbol{S}_1)p\uparrow\rangle|\phi(\boldsymbol{S}_1)p\downarrow\rangle|\phi(\boldsymbol{S}_1)n\uparrow\rangle|\phi(\boldsymbol{S}_1)n\downarrow\rangle \\ &\times|\phi(\boldsymbol{S}_2)p\uparrow\rangle|\phi(\boldsymbol{S}_2)n\uparrow\rangle|\phi(\boldsymbol{S}_2)n\downarrow\rangle\}. \end{aligned} \tag{2}$$

Here $\phi(\boldsymbol{S}_i)$ is the $0s$ wave function shifted to the position $\boldsymbol{S}_i$, and $|\psi_{1\tau}(\boldsymbol{S}_1)\rangle$ and $|\psi_{2\tau}(\boldsymbol{S}_1)\rangle$ indicate p-shell orbits for the neutron configurations labeled by $\tau = \{a,b,c,d,e,f\}$ of the ^{6}He cluster shifted to $\boldsymbol{S}_1$. Schematic configurations for $\tau = \{a,b,c,d,e,f\}$ are illustrated in Fig. 1.

The ls coupling configurations are given by the configurations $\tau = a$, b, and c, in which two-neutron orbits are written by rotated configurations of $|p_y,n\uparrow\rangle_{\boldsymbol{S}_1}|p_y,n\downarrow\rangle_{\boldsymbol{S}_1}$ as

$$|\psi_{1\tau}(\boldsymbol{S}_1)\rangle = \hat{R}_{x,\boldsymbol{S}_1}(\theta)|p_y,n\uparrow\rangle_{\boldsymbol{S}_1}, \tag{3}$$

$$|\psi_{2\tau}(\boldsymbol{S}_1)\rangle = \hat{R}_{x,\boldsymbol{S}_1}(\theta)|p_y,n\downarrow\rangle_{\boldsymbol{S}_1}, \tag{4}$$

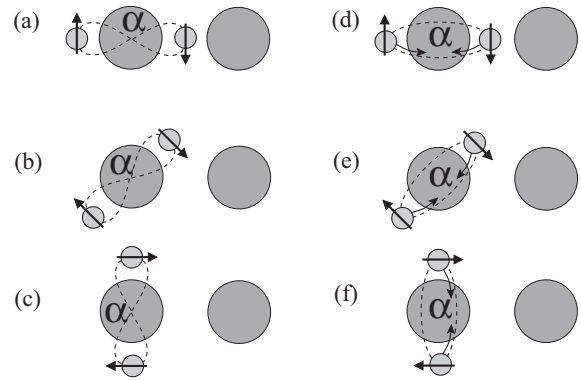

FIG. 1. Schematic configurations for (a)–(f) of the ^{6}He cluster in the ^{6}He + t and ^{6}He + α cluster models. Details are described in the text. The figure is taken from Ref. [52].

with the rotational angle $\theta = \pi/2$, $\theta = \pi/4$, and $\theta = 0$, respectively. Here, $\hat{R}_{x,\boldsymbol{S}_1}(\theta)$ is the rotation operator around the x-oriented axis passing through $\boldsymbol{S}_1$.

The $p^2_{3/2}$ configurations in the jj coupling scheme are described by the configurations $\tau = d$, e, and f, in which two neutron orbits are given by rotated configurations of $|p_{(+)},n\uparrow\rangle_{\boldsymbol{S}_1}|p_{(-)},n\downarrow\rangle_{\boldsymbol{S}_1}$ as

$$|\psi_{1\tau}(\boldsymbol{S}_1)\rangle = \hat{R}_{x,\boldsymbol{S}_1}(\theta)|p_{(+)},n\uparrow\rangle_{\boldsymbol{S}_1}, \tag{5}$$

$$|\psi_{2\tau}(\boldsymbol{S}_1)\rangle = \hat{R}_{x,\boldsymbol{S}_1}(\theta)|p_{(-)},n\downarrow\rangle_{\boldsymbol{S}_1}, \tag{6}$$

where $\theta = \pi/2$, $\theta = \pi/4$, and $\theta = 0$ are chosen for d, e, and f, respectively.

In the GCM calculation, the ^{6}He + $\alpha(t)$ cluster wave functions are superposed as

$$\left|\Psi^{J^\pi_k}_M\right\rangle = \sum_D \sum_{\tau,K} c^{(J^\pi_k)}_{D,\tau,K} P^{J\pi}_{MK}|\Phi_\tau(D)\rangle, \tag{7}$$

where the coefficients $c^{(J^\pi_k)}_{D,\tau,K}$ are determined by diagonalizing norm and Hamiltonian matrices. I use the generator coordinate $D \leqslant D_{\max}$ in order to obtain wave functions for resonance states as bound-state solutions.

The present model space given by the K-projected wave functions of six configurations fully covers all p-shell configurations of 0^+ and 2^+ states of the ^{6}He cluster located at an intercluster distance D. A single configuration has a deformed ^{6}He cluster with a specific orientation, indicating a strong-coupling cluster structure, in which the angular momenta of the clusters and that of intercluster motion are strongly coupled. At moderate distance D, configuration (a) with two neutrons in the longitudinal direction approximately corresponds to the molecular orbital σ^2 structure (this is a result of the antisymmetrization effect), which dominates the ^{10}Be(0^+_2) state consistently with preceding works [4,6–15,17,20,23]. On the other hand, in the asymptotic region at a large distance D, the system goes into a weak-coupling cluster state, in which the ^{6}He subsystem becomes its energy eigenstate with a specific spin I. The current framework takes the transition from strong- to weak-coupling cluster structures into account by means of a linear combination of configurations (a)–(f) projected to the total angular-momentum eigenstates. This expression is useful

for analyzing the cluster structures of $^6\mathrm{He}+\alpha(t)$ in $^{10}\mathrm{Be}(^9\mathrm{Li})$, in particular in a strong-coupling regime.

The transition between the strong- and weak-coupling cluster structures of ^{10}Be was presented by Ito *et al.* [20,23] using the GTCM; in their formulation, molecular orbital configurations are fully taken into account via channel coupling (configuration mixing) of the $^5\mathrm{He}+^5\mathrm{He}$ channel with the $^6\mathrm{He}+\alpha$ channel. In this work, I omit the coupling with the $^5\mathrm{He}+^5\mathrm{He}$ channel in order to reduce the number of basis wave functions. Despite omitting the $^5\mathrm{He}+^5\mathrm{He}$ configurations, this method well describes the experimental energy spectra of the $K=0_1^+$, $K=2_1^+$, and $K=0_2^+$ bands of ^{10}Be as is already shown in my previous work [52].

In the practical calculation, I express a configuration of the $^6\mathrm{He}+\alpha(t)$ wave functions with a single antisymmetrized molecular dynamics (AMD) wave function given by a Slater determinant of single-particle Gaussian wave packets. The general form of AMD wave functions is described, for example, in Refs. [2,3,55].

B. Isoscalar monopole transitions

The isoscalar monopole (ISM) operator $\mathcal{M}(IS0)$ is defined as

$$\mathcal{M}(IS0)=\sum_i(\boldsymbol{r}_i-\boldsymbol{R})^2, \tag{8}$$

where $\boldsymbol{r}_i$ is the ith nucleon coordinate and $\boldsymbol{R}$ is the center-of-mass coordinate $\boldsymbol{R}\equiv\sum_i \boldsymbol{r}_i/A$. The ISM strength from the ground state to an excited state (J_k^π) is given by the reduced matrix element of the ISM operator as

$$B\left(IS0;\mathrm{g.s.}\rightarrow J_k^\pi\right)=\frac{1}{2J+1}\left|\langle\mathrm{g.s.}||\mathcal{M}(IS0)||J_k^\pi\rangle\right|^2. \tag{9}$$

The energy-weighted sum (EWS) of the ISM strengths is defined as

$$S(IS0)\equiv\sum_k(E_k-E_{\mathrm{g.s.}})B\left(IS0;\mathrm{g.s.}\rightarrow J_k^\pi\right). \tag{10}$$

If the interaction commutes with $\mathcal{M}(\mathrm{IS0})$, then the ISM energy-weighted sum rule (EWSR)

$$S(IS0)=\frac{2\hbar^2}{m}A\langle r^2\rangle_{\mathrm{g.s.}} \tag{11}$$

is satisfied. Here $\langle r^2\rangle_{\mathrm{g.s.}}$ is the mean-square radius of the ground state and is equal to $\langle\mathrm{g.s.}|\mathcal{M}(IS0)|\mathrm{g.s.}\rangle/A$.

C. Overlap with reference $^6\mathrm{He}+\alpha(t)$ wave functions with D

To analyze the cluster structures of $^{10}\mathrm{Be}(0^+)$ and $^9\mathrm{Li}(3/2^-)$ obtained by GCM calculation, I calculate overlaps with two types of reference $^6\mathrm{He}+\alpha(t)$ wave functions at a given distance D: $^6\mathrm{He}(I^+)+\alpha(t)$ wave functions with angular-momentum coupling $[I\otimes J']_J$, and the basis wave functions $\Phi_\tau(D)$ used in the GCM calculation. The former is a weak-coupling $^6\mathrm{He}+\alpha(t)$ wave function, in which the internal angular momenta of clusters and the orbital angular momentum of intercluster motion are weakly coupled, whereas the latter is a strong-coupling $^6\mathrm{He}+\alpha(t)$ wave function, in which a deformed ^{6}He cluster is oriented to a specific angle from the $\alpha(t)$ direction.

The $^6\mathrm{He}(I^+)+\alpha(t)$ wave functions are constructed using the ground and first-excited states $^6\mathrm{He}(0^+)$ and $^6\mathrm{He}(2^+)$ of an isolated ^{6}He cluster described by ho p-shell configurations. The $^6\mathrm{He}(I^+)+\alpha(t)$ wave functions at distances D are given by a linear combination of the basis wave functions $P^{J\pi}_{MK}|\Phi_\tau(D)\rangle$ used in the present model and are defined as

$$\Phi^{[I\otimes J']_J}_{^6\mathrm{He}+\alpha(t)}(D)=n_0\mathcal{A}\left\{\phi_{\mathrm{G}}(\boldsymbol{R})\gamma_l(D;r)\left[\varphi_I^{^6\mathrm{He}}\left[\varphi_{I'}^{\alpha(t)}Y_l(\hat{r})\right]_{J'}\right]_J\right\}, \tag{12}$$

$$\gamma_l(D;r)\equiv 4\pi\left(\frac{2\tilde{\nu}}{\pi}\right)^{\frac{3}{4}}i_l(2\tilde{\nu}Dr)e^{-\tilde{\nu}(r^2+D^2)}, \tag{13}$$

$$\tilde{\nu}\equiv\frac{A_1A_2}{A}\nu, \tag{14}$$

$$\phi_{\mathrm{G}}(\boldsymbol{R})=\left(\frac{2A\nu}{\pi}\right)e^{-A\nu\boldsymbol{R}^2}, \tag{15}$$

where i_l is the modified spherical Bessel function; $\varphi_I^{^6\mathrm{He}}$ and $\varphi_{I'}^{\alpha(t)}$ represent the internal wave functions of $^6\mathrm{He}(I^+)$ and $\alpha(t)$ clusters with the internal angular momentum I and I', respectively; ϕ_G is the wave function of the center of mass motion; and n_0 is the normalization factor.

For the strong-coupling $^6\mathrm{He}+\alpha(t)$ wave functions, I consider the J^π and K projected states of the basis wave functions $\Phi_\tau(D)$ with the following specific configurations:

$$\Phi^{(T)}_{^6\mathrm{He}+\alpha(t)}(D)\equiv n_0P^{J\pi}_{M0(1/2)}|\Phi_{\tau=f}(D)\rangle, \tag{16}$$

$$\Phi^{(A)}_{^6\mathrm{He}+\alpha(t)}(D)\equiv n_0P^{J\pi}_{M0(1/2)}|\Phi_{\tau=a}(D)\rangle, \tag{17}$$

$$\Phi^{(I_z2)}_{^6\mathrm{He}+t}(D)\equiv n_0P^{J\pi}_{M,-3/2}|\Phi_{\tau=c}(D)\rangle, \tag{18}$$

where $\Phi^{(T)}_{^6\mathrm{He}+\alpha(t)}(D)$ is the jj coupling transverse (T) configuration corresponding to the configuration (f) with two neutrons in the transverse orbits with $|j_z|=3/2$, and $\Phi^{(A)}_{^6\mathrm{He}+\alpha(t)}(D)$ is the ls coupling aligned (A) configuration given by configuration (a) with two neutrons coupling to $S=0$ in the aligned orbit p_z. In the short-distance region, $\Phi^{(T)}_{^6\mathrm{He}+\alpha(t)}(D)$ feels a weaker Pauli blocking effect than other configurations. Configuration (a), i.e., $\Phi^{(A)}_{^6\mathrm{He}+\alpha(t)}(D)$ with a moderate distance parameter D, corresponds to the molecular σ-orbital structure. $\Phi^{(I_z2)}_{^6\mathrm{He}+t}(D)$ is the $K=-3/2$ state projected from the ls coupling transverse configuration given by configuration (c), where the rotation of a $S=0$ two-neutron pair in the ^{6}He cluster contributes to $I_z=-2$.

The defined weak- and strong-coupling reference wave functions, $\Phi^{[I\otimes J']_J}_{^6\mathrm{He}+\alpha(t)}(D)$ and $\Phi^{(T,A,I_z2)}_{^6\mathrm{He}+\alpha(t)}(D)$, are not orthogonal to each other. In Fig. 2, I show squared overlaps of $\Phi^{[I\otimes J']_J}_{^6\mathrm{He}+\alpha(t)}(D)$ with $\Phi^{(T,A,I_z2)}_{^6\mathrm{He}+\alpha(t)}(D)$. In the short-distance region, only transverse configurations are Pauli allowed while other configurations feel strong Pauli blocking due to the antisymmetrization between valence neutrons and the $\alpha(t)$ cluster. As a result, both $^6\mathrm{He}(0^+)+\alpha$ and $^6\mathrm{He}(2^+)+\alpha$ wave functions, $\Phi^{[0\otimes0]_0}_{^6\mathrm{He}+\alpha}(D)$ and $\Phi^{[2\otimes2]_0}_{^6\mathrm{He}+\alpha}(D)$, have dominant overlaps with

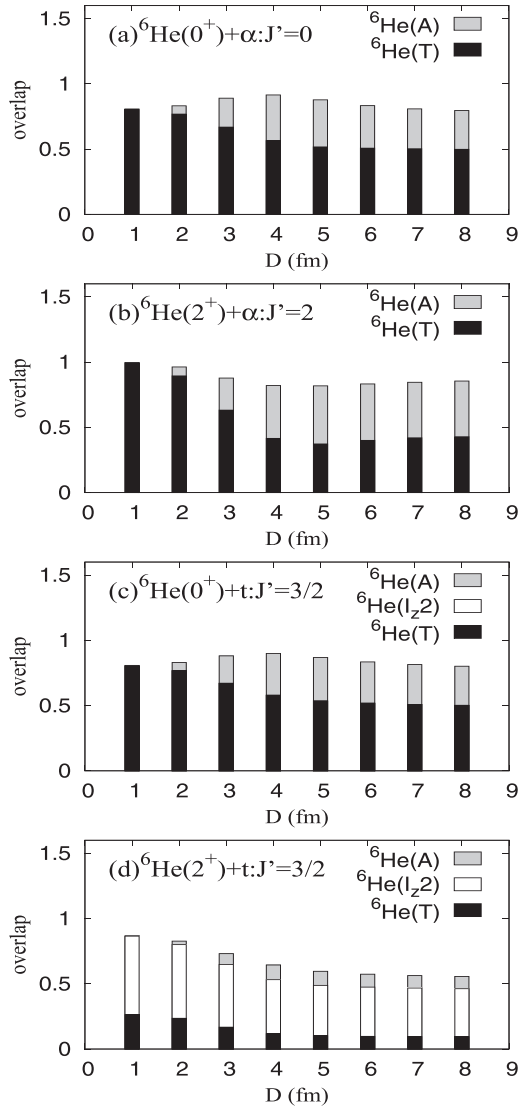

FIG. 2. Squared overlaps between the weak-coupling cluster wave functions $\Phi^{[I\otimes J']_J}_{^6\mathrm{He}+\alpha(t)}(D)$ and the strong-coupling cluster wave functions $\Phi^{(T,A,I_z2)}_{^6\mathrm{He}+\alpha(t)}(D)$. The squared overlaps of (a) $\Phi^{[0\otimes0]_0}_{^6\mathrm{He}+\alpha}(D)$, (b) $\Phi^{[2\otimes2]_0}_{^6\mathrm{He}+\alpha}(D)$, (c) $\Phi^{[0\otimes3/2]_{3/2}}_{^6\mathrm{He}+t}(D)$, and (d) $\Phi^{[0\otimes3/2]_{3/2}}_{^6\mathrm{He}+t}(D)$ with $\Phi^{(T,A,I_z2)}_{^6\mathrm{He}+\alpha(t)}(D)$ are shown.

the transverse configuration $\Phi^{(T)}_{^6\mathrm{He}+\alpha}(D)$ but no overlap with the aligned configuration $\Phi^{(A)}_{^6\mathrm{He}+\alpha}(D)$. This means that the ^{6}He(0$^+$) + α and ^{6}He(2$^+$) + α wave functions at a short distance are almost equivalent to the $\Phi^{(T)}_{^6\mathrm{He}+\alpha}(D)$ wave function and contain no $\Phi^{(A)}_{^6\mathrm{He}+\alpha}(D)$ component. As for the ^{6}He + t wave functions at a short distance D, the ^{6}He(0$^+$) + t wave function is almost equivalent to $\Phi^{(T)}_{^6\mathrm{He}+t}(D)$, the ^{6}He(2$^+$) + t wave function is a mixing of $\Phi^{(T)}_{^6\mathrm{He}+t}(D)$ and $\Phi^{(I_z3/2)}_{^6\mathrm{He}+t}(D)$, and neither contains a $\Phi^{(A)}_{^6\mathrm{He}+t}(D)$ component. This is a trivial consequence of the antisymmetrization of the ^{6}He + α cluster wave functions and indicates that, at short distances, the weak-coupling ^{6}He + $\alpha(t)$ wave functions have less physical meaning than the strong-coupling ^{6}He + $\alpha(t)$ wave functions. At a sufficiently large distance D free from the Pauli blocking between two clusters, $\Phi^{[I\otimes J']_J}_{^6\mathrm{He}+\alpha(t)}(D)$ with different I and J' are orthogonal to each other and have overlaps with $\Phi^{(T,A,I_z2)}_{^6\mathrm{He}+\alpha(t)}(D)$ in specific ratios.

III. RESULTS

A. Effective nuclear forces

The effective Hamiltonian consists of the single-particle kinetic terms t_i and the two-body forces v_{ij} containing the effective nuclear forces and the Coulomb force:

$$H_{\mathrm{eff}} = \sum_i t_i - T_G + \sum_{i<j} v_{ij}, \tag{19}$$

where T_G, the kinetic energy of the center-of-mass motion, is subtracted. In terms of the effective nuclear forces, the Volkov No. 2 force [56] is used as the central force, and the spin-orbit term of the G3RS force [57] is adopted for the spin-orbit force, as done in preceding studies on ^{10}Be and ^{9}Li structures [10,13,14,52,58]. The interaction parameters are ($b = h = 0.125, m = 0.60$) for the Volkov No. 2 force and $u_{\mathrm{I}} = -u_{\mathrm{II}} = 1600$ MeV for the strength of the spin-orbit force; these are the same as those used in Refs. [52,58]. The Coulomb force is approximated by seven-range Gaussians.

B. Energy levels of ^{9}Li and ^{10}Be

As described in Eq. (7), the ^{6}He + $\alpha(t)$ cluster wave functions $|\Phi_\tau(D)\rangle$ specified by the label τ and the distance parameter D are superposed. In the default GCM calculation, I take the generator coordinate, $D = 1,2,\ldots,8$ fm, which corresponds to a bound-state approximation. To observe resonance features, I also use a larger model space, $D = 1,2,\ldots,15$ fm, to examine the effect of coupling with discretized continuum states. The six configurations, τ={a,b,c,d,e,f}, are adopted at each D, and a total of $6 \times 8 = 48 (6 \times 15 = 90)$ basis wave functions are superposed in the $D = 1,2,\ldots,8$ fm ($D = 1,2,\ldots,15$ fm) calculation, which I denote the "$D \leqslant 8$ ($D \leqslant 15$)" calculation. In the $D \leqslant 8$ and $D \leqslant 15$ calculations, K-mixing is taken into account. In addition, I perform the GCM calculation with a truncated model space using only the transverse configurations, (c) and (f), which are denoted as the "(c+f)" calculation. In the (c+f) calculation, the angular-momentum-projected ^{6}He + $\alpha(t)$ wave functions of the configurations, (c) and (f), with $K = 0(1/2)$ and $D = 1,2,\ldots,8$ fm are used.

Figure 3 shows the energy spectra of ^{10}Be(0$^+$) and ^{9}Li(3/2$^-$) obtained using the default $D \leqslant 8$ calculation. The ^{6}He + α and ^{6}He + t threshold energies are shown by dashed lines. The ^{10}Be($0^+_{3,4}$) and ^{9}Li($3/2^-_{3,4,5}$) states are obtained above the ^{6}He + α and ^{6}He + t threshold energies, respectively. The ^{10}Be(0^+_3) and ^{10}Be(0^+_4) states have relatively larger ^{6}He(0$^+$) + α and ^{6}He(2$^+$) + α components, respectively. The ^{9}Li($3/2^+_3$) state is dominated by the ^{6}He(0$^+$) + t component, while ^{9}Li($3/2^+_4$) and ^{9}Li($3/2^+_5$) have dominant ^{6}He(2$^+$) + t components. The dominant ^{6}He + $\alpha(t)$ components decrease at the boundary, $D = 8$ fm, and therefore these states are regarded

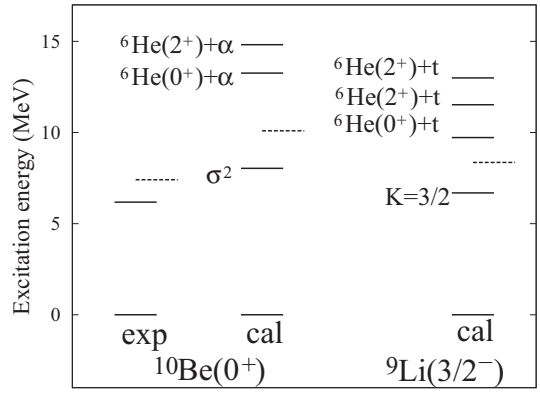

FIG. 3. Energy levels of ^{10}Be(0$^+$) and ^{9}Li(3/2$^-$) obtained using the $D \leqslant 8$ calculation. The experimental energy levels of ^{10}Be(0$^+$) are also shown. The ^{6}He + α and ^{6}He + t threshold energies are shown as dashed lines.

as resonance states. States higher than the ^{10}Be(0^+_4) and ^{9}Li($3/2^+_5$) states do not show such resonance features and are regarded as continuum states. In the low-energy region of ^{10}Be, the 0^+_2 state of ^{10}Be with the molecular σ-orbital structure is obtained below the threshold energy. This state is the band-head state of the $K^\pi = 0^+_2$ band and is assigned as the experimental 0^+ state at 6.18 MeV. However, in ^{9}Li, the molecular orbital structure does not appear because the σ-orbital is unfavored around the $\alpha + t$ core due to the asymmetry of the core potential as discussed in my previous work. The ^{9}Li($3/2^-_2$) state obtained below the ^{6}He + t threshold energy is the band-head state of the $K^\pi = 3/2^-$ band.

In the $D \leqslant 8$ calculation, the resonance states are obtained as bound-state solutions in the model space of $D \leqslant 8$ fm. I estimate the partial decay widths $\Gamma_{I\otimes J'}$ of the resonance states for ^{6}He(I^+) + $\alpha(t)$ channels with angular-momentum coupling $[I \otimes J']_J$ from the reduced width amplitude $y(a)$ at a channel radius a as described in Appendix. Here J' is the resultant angular momentum of the angular momenta I' and l, where I' is the internal angular momentum of the $\alpha(t)$ cluster and l is the orbital angular momentum for the relative coordinate $\boldsymbol{r}$ between centers of mass of two clusters. For ^{6}He(0$^+$) + α and ^{6}He(2$^+$) + α decays of ^{10}Be(0$^+$), S- and D-wave decays in the $[I \otimes J']_J = [0 \otimes 0]_0$ and $[2 \otimes 2]_0$ channels are calculated, respectively. For ^{6}He(0$^+$) + t and ^{6}He(2$^+$) + t decays of ^{9}Li(3/2$^-$), I consider P-wave decays in three channels, $[0 \otimes 3/2]_{3/2}$, $[2 \otimes 3/2]_{3/2}$, and $[2 \otimes 1/2]_{3/2}$.

The calculated partial decay widths $\Gamma_{I\otimes J'}$ at channel radii $a = 5$, 6, and 7 fm are shown in Table I. Here, the decay energies ($E_{\rm decay}$) are calculated from the theoretical energies of t, α, ^{6}He(0$^+$,2$^+$), ^{10}Be, and ^{9}Li. The sum $\Gamma_{\rm sum}$ of the partial widths and the dimensionless reduced widths $\theta^2(a) = (a/3)|ay(a)|^2$ are also shown in the table. Hereafter, I discuss the decay widths calculated at the channel radius that gives the largest $\Gamma_{\rm sum}$ for each state. The calculated width of ^{10}Be(0^+_3) is $\Gamma_{\rm sum} = 1.6$ MeV for the dominant ^{6}He(0$^+$) + α decay and that of ^{10}Be(0^+_4) is $\Gamma_{\rm sum} = 1.0$ MeV with comparable partial widths of ^{6}He(0$^+$) + α and ^{6}He(2$^+$) + α decays. The calculated widths of ^{9}Li($3/2^-_3$), ^{9}Li($3/2^-_4$), and ^{9}Li($3/2^-_5$) are $\Gamma_{\rm sum} = 0.65$, 0.75, and 2.0 MeV, respectively. The ^{9}Li($3/2^-_3$) state can decay only in the ^{6}He(0$^+$) + t channel because the ^{6}He(2$^+$) + t channel is closed. ^{9}Li($3/2^-_4$) has comparable partial widths of ^{6}He(0$^+$) + t and ^{6}He(2$^+$) + t decays, whereas ^{9}Li($3/2^-_5$) has dominant ^{6}He(2$^+$) + t decays.

TABLE I. Partial decay widths $\Gamma_{I\otimes J'}$ (MeV) for ^{6}He(I^+) + α of ^{10}Be(0$^+$) and ^{6}He(I^+) + t of ^{9}Li(3/2$^-$) obtained by the $D \leqslant 8$ calculation. $\Gamma_{I\otimes J'}$ for S-wave and D-wave decays in $[0 \otimes 0]_0$ and $[2 \otimes 2]_0$ of ^{10}Be(0$^+$) and P-wave decays in $[0 \otimes 3/2]_{3/2}$, $[2 \otimes 3/2]_{3/2}$, and $[2 \otimes 1/2]_{3/2}$ of ^{9}Li(3/2$^-$) are shown. The sum ($\Gamma_{\rm sum}$) of the partial widths and the dimensionless reduced widths $\theta^2(a) = (a/3)|ay(a)|^2$ are also shown.

a (fm)	$E_{\rm decay}$ (MeV)	θ^2			$\Gamma_{I\otimes J'}$ (MeV)		
		5	6	7	5	6	7
^{6}He(0$^+$) + α with $[0 \otimes 0]_0$							
^{10}Be(0^+_3)	3.2	0.04	0.20	0.38	0.18	0.92	1.55
^{10}Be(0^+_4)	4.7	0.02	0.01	0.10	0.14	0.05	0.54
^{6}He(2$^+$) + α with $[2 \otimes 2]_0$							
^{10}Be(0^+_3)	1.3	0.13	0.12	0.08	0.011	0.02	0.02
^{10}Be(0^+_4)	2.9	0.07	0.19	0.23	0.10	0.34	0.49
^{6}He(0$^+$) + t with $[0 \otimes 3/2]_{3/2}$							
^{9}Li($3/2^-_3$)	1.4	0.26	0.33	0.29	0.59	0.75	0.65
^{9}Li($3/2^-_4$)	3.2	0.01	0.04	0.06	0.08	0.21	0.30
^{9}Li($3/2^-_5$)	4.6	0.000	0.001	0.004	0.000	0.007	0.02
^{6}He(2$^+$) + t with $[2 \otimes 3/2]_{3/2}$							
^{9}Li($3/2^-_4$)	1.3	0.13	0.15	0.13	0.30	0.33	0.27
^{9}Li($3/2^-_5$)	2.8	0.06	0.15	0.20	0.33	0.69	0.86
^{6}He(0$^+$) + t with $[2 \otimes 1/2]_{3/2}$							
^{9}Li($3/2^-_4$)	1.3	0.09	0.10	0.08	0.19	0.21	0.18
^{9}Li($3/2^-_5$)	2.8	0.09	0.20	0.27	0.44	0.93	1.15
	E_r (MeV)	$\Gamma_{\rm sum}$ (MeV)					
^{10}Be(0^+_3)	3.2	0.19	0.93	1.6			
^{10}Be(0^+_4)	4.7	0.24	0.39	1.0			
^{9}Li($3/2^-_3$)	1.4	0.59	0.75	0.65			
^{9}Li($3/2^-_4$)	3.2	0.57	0.75	0.75			
^{9}Li($3/2^-_5$)	4.6	0.77	1.6	2.0			

To observe the resonance features of these states obtained above the threshold energies, I perform the $D \leqslant 15$ calculation with a larger model space than that of the $D \leqslant 8$ calculation. In a model space that has been enlarged from $D \leqslant 8$ fm to $D \leqslant 15$ fm, the resonance states $|\Psi^{J^\pi_k}_{D\leqslant 8}\rangle$, which are obtained as bound-state solutions in the $D \leqslant 8$ calculation, couple with discretized continuum states and their components are fragmented into states ($|\Psi^{J^\pi_l}_{D\leqslant 15}\rangle$). In Fig. 4, I show the squared overlap $|\langle\Psi^{J^\pi_k}_{D\leqslant 8}|\Psi^{J^\pi_l}_{D\leqslant 15}\rangle|^2$. The overlap distributions show that the components of the resonance states obtained by the $D \leqslant 8$ calculation are fragmented into several states in the $D \leqslant 15$ calculation, whereas those of the ^{10}Be(0^+_2) and ^{9}Li($3/2^+_2$) below the threshold energies are not fragmented. As shown in the figure, the overlap distributions are consistent with the Breit-Wigner distributions at the resonance energies with widths ($\Gamma_{\rm sum}/2$) obtained by the $D \leqslant 8$ calculation. This result indicates that the decay widths $\Gamma_{\rm sum}$ estimated using the reduced width amplitudes are reasonable.

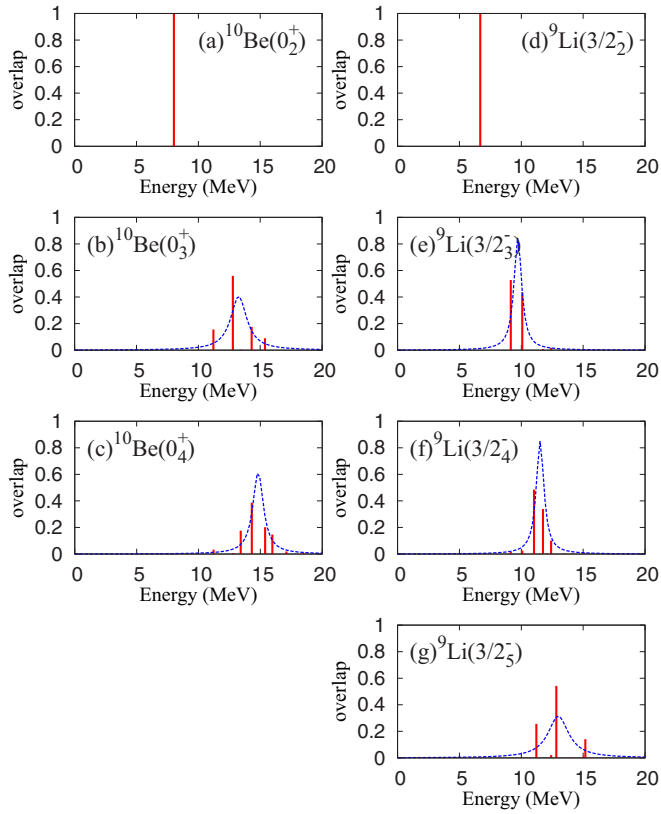

FIG. 4. Distributions of the squared overlap $|\langle\Psi^{J^\pi_k}_{D\leqslant 8}|\Psi^{J^\pi_i}_{D\leqslant 15}\rangle|^2$ of the J_k state obtained by the $D \leqslant 8$ calculation with states obtained using the $D \leqslant 15$ calculation. Distributions of the $J_k = 0^+_2, 0^+_3$, and 0^+_4 states in ^{10}Be are shown in (a)–(c), and those of $J_k = 3/2^-_2, 3/2^-_3, 3/2^-_4$, and $3/2^-_5$ states in ^{9}Li are shown in (d)–(g). The Breit-Wigner distributions at energies (E_x) with widths ($\Gamma_{\rm sum}/2$) for the resonances obtained by the $D \leqslant 8$ calculation are shown by dashed lines. The largest value of $\Gamma_{\rm sum}$ at $a = 5$, 6, and 7 fm from Table I is adopted for each state.

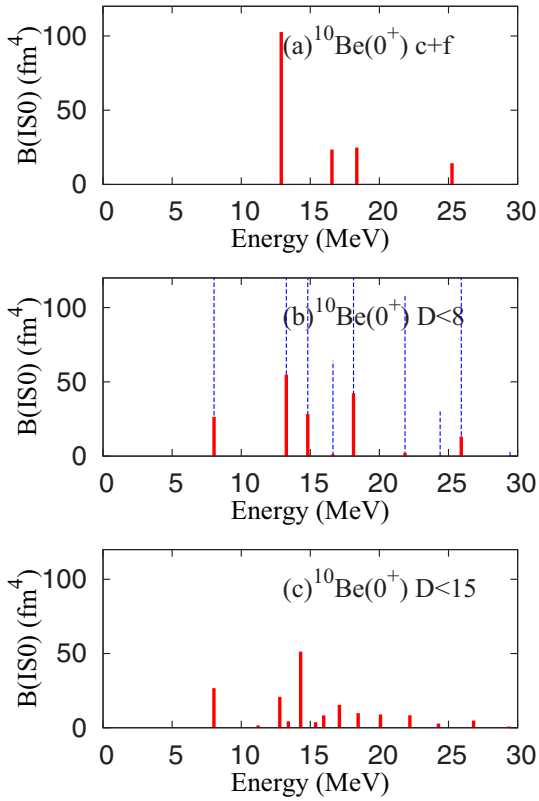

FIG. 5. ISM strength distributions of ^{10}Be(0^+) obtained by the (c+f), $D \leqslant 8$, and $D \leqslant 15$ calculations. Dashed lines in the middle panel (b) for the $D \leqslant 8$ calculation show 50-fold values of the strengths.

Ito *et al.* investigated ^{6}He + α cluster resonances and molecular orbital states in ^{10}Be using the GTCM calculation, which predicts a ^{6}He(2^+) + α resonance at the energy E_r = 3.6 MeV relative to the ^{6}He + α threshold energy and a ^{6}He(0^+) + α state as a broad continuum state in the E_r = 1–4 region. My result of ^{10}Be(0^+_4) with a dominant ^{6}He(2^+) + α component may correspond to the ^{6}He(2^+) + α state of the GTCM. The ^{10}Be(0^+_3) state obtained in the present result, which has a dominant ^{6}He(0^+) + α component and a larger width than the ^{10}Be(0^+_4) state, is likely to correspond to the ^{6}He(0^+) + α state of the GTCM.

C. Isoscalar monopole transition strengths

The ISM transition strengths of ^{10}Be(0^+) and ^{9}Li($3/2^-$) calculated by the (c+f), $D \leqslant 8$, and $D \leqslant 15$ calculations are shown in Figs. 5 and 6, respectively. The energy-weighted ISM strengths and their Gaussian smeared distributions are shown in Fig. 7. The proton and matter radii, EWSR, EWS, and the ratio EWS/EWSR obtained in the (c+f), $D \leqslant 8$, and $D \leqslant 15$ calculations are listed in Table II. The experimental radii are also shown in the table. In the (c+f) calculation, the model space is truncated and contains only the configurations (c) and (f), which corresponds to the transverse configurations of ^{6}He with two neutrons in p_x or p_y orbits. Despite the truncation of ^{6}He configurations, the EWS of the (c+f) result is consistent with those of the $D \leqslant 8$ and $D \leqslant 15$ calculations, as both the ground state $|$g.s.$\rangle$ and its $\mathcal{M}(IS0)$ operated state $\mathcal{M}(IS0)|$g.s.$\rangle$ are contained in the truncated model space of the transverse configurations (c) and (f).

The ISM strength for ^{10}Be, obtained using the (c+f) calculation, is concentrated on the first excited state at $E_x \sim$ 13 MeV. In the $D \leqslant 8$ result, the ISM strengths are split by coupling with other configurations (a), (b), (d), and (e). However, significant strengths remain for the transitions to ^{10}Be(0^+_3) and ^{10}Be(0^+_4) states for E_x = 13–15 MeV. In the $D \leqslant 15$ result, the strengths are fragmented further due to coupling with the continuum states but are still concentrated in the E_x = 13–15 MeV region for ^{10}Be(0^+_3) and ^{10}Be(0^+_4) states. In the energy-weighted strength distributions shown in Fig. 7(c), the enhancement of the ISM strengths are found in this energy region. This result indicates that ISM excitation can be a good probe for observing ^{6}He + α cluster resonances in ^{10}Be. The ISM strength for ^{10}Be(0^+_2) is not as significant as those in the E_x = 13–15 MeV region.

For ^{9}Li, the ISM strength obtained by the (c+f) calculation is somewhat concentrated on the first excited state at

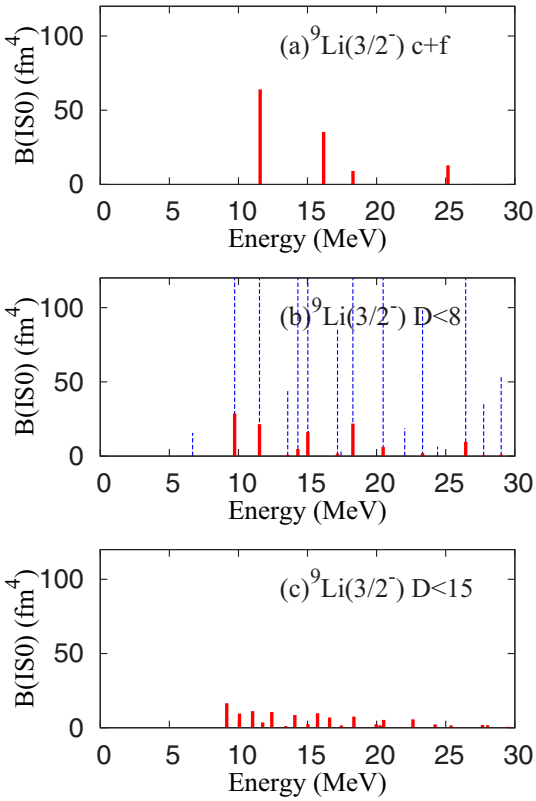

FIG. 6. ISM strength distributions of ^{9}Li($3/2^-$) obtained by the (c+f), $D \leqslant 8$, and $D \leqslant 15$ calculations. Dashed lines in the middle panel (b) for the $D \leqslant 8$ calculation show 50-fold values of the strengths.

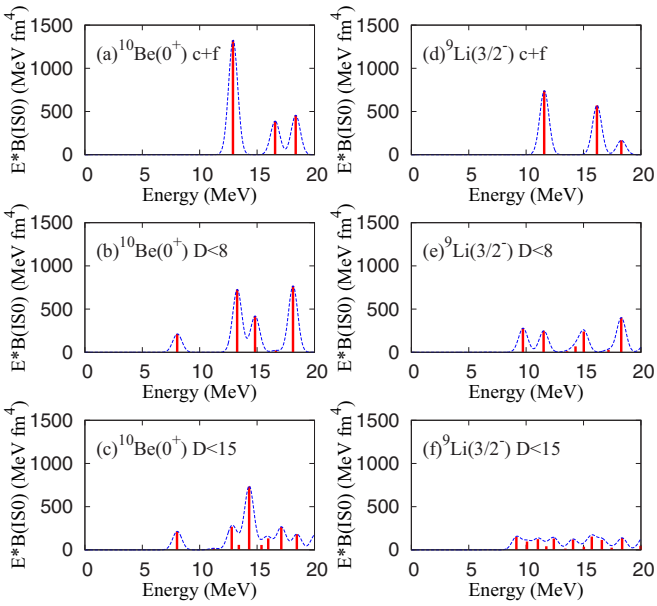

FIG. 7. Energy-weighted ISM strengths (solid lines). Panels (a)–(c) show the distributions in ^{10}Be(0$^+$) obtained by the (c+f), $D \leqslant 8$, $D \leqslant 15$ calculations, and panels (d)–(f) show the distributions in ^{9}Li($3/2^-$). The Gaussian smeared distributions of the energy-weighted ISM strengths with fixed width $1/\sqrt{\pi}$ are shown by dashed lines.

TABLE II. Theoretical values of proton and matter radii (fm), EWSR (MeV fm^4), EWS (MeV fm^4), and ratio EWS/EWSR of the ISM strengths obtained using the $D \leqslant 8$ calculation. The experimental proton radii reduced from the charge radii [59,60], and the experimental matter radii deduced from the interaction cross sections [61] are also shown.

	^{10}Be				
	r_p	r_m	EWSR	EWS	EWS/EWSR
(c+f)	2.31	2.33	4.5×10^2	2.7×10^2	0.60
$D \leqslant 8$	2.31	2.34	4.5×10^2	2.7×10^2	0.61
$D \leqslant 15$	2.31	2.34	4.5×10^2	2.7×10^2	0.61
exp.	2.221(18)	2.30(2)			
			^{9}Li		
(c+f)	2.12	2.23	3.7×10^2	1.68×10^2	0.45
$D \leqslant 8$	2.11	2.22	3.7×10^2	1.68×10^2	0.46
$D \leqslant 15$	2.11	2.22	3.7×10^2	1.68×10^2	0.46
Exp.	2.05(4)	2.32(2)			

$E_x \sim 11$ MeV, but the magnitude of the strength is not as significant in the ^{10}Be case. In the $D \leqslant 8$ result, the strength distributions are fragmented due to the mixing of other configurations (a), (b), (d), and (e), and in the $D \leqslant 15$ result, they are strongly scattered due to coupling with continuum states. The stronger fragmentation of ISM strengths in ^{9}Li than in ^{10}Be originates in various angular-momentum channels $[I \times J']$ and in K-mixing in the total spin-parity $J^\pi = 3/2^-$ of final states. Consequently, there is no concentration of ISM strengths in the ^{6}He + t cluster resonances in ^{9}Li. Indeed, as shown in Fig. 7(e), the energy-weighted strengths are widely distributed and the resonance states in ^{9}Li do not have significant strength. ^{9}Li($3/2^-_2$) has nearly no ISM strength, as this state is the band-head state of the $K^\pi = 3/2^-$ band and is not excited by the ISM operator from the ^{9}Li ground state, which has the dominant $K^\pi = 1/2^-$ component.

IV. DISCUSSIONS

In this section, I discuss the cluster structures of ^{10}Be(0$^+$) and ^{9}Li($3/2^-$) in connection with ISM excitations. By analyzing the overlaps of the obtained ^{10}Be(0$^+$) and ^{9}Li($3/2^-$) wave functions with the reference ^{6}He + $\alpha(t)$ wave functions, cluster aspects can be examined from two viewpoints of weak- and strong-coupling cluster pictures.

A. Cluster structures of ^{10}Be(0$^+$) and ^{9}Li($3/2^-$)

In order to discern the cluster components of the obtained ^{10}Be(0$^+$) and ^{9}Li($3/2^-$) states, I calculate the overlaps with the reference ^{6}He + $\alpha(t)$ wave functions at distances D, $\Phi^{[I\otimes J']J}_{^6\mathrm{He}+\alpha(t)}(D)$, and $\Phi^{(T,A,I_2)}_{^6\mathrm{He}+\alpha(t)}(D)$. Figures 8 and 9 show the squared overlaps of the ^{10}Be(0$^+$) and ^{9}Li($3/2^-$) states obtained using the $D \leqslant 8$ calculation with the ^{6}He + $\alpha(t)$ wave functions plotted as functions of D.

The ^{10}Be ground state has a dominant overlap with the transverse configuration $\Phi^{(T)}_{^6\mathrm{He}+\alpha}(D)$ at $D \sim 3$ fm and has almost no overlap with the aligned configuration $\Phi^{(A)}_{^6\mathrm{He}+\alpha}(D)$. ^{10}Be($0^+_2$) is dominated by $\Phi^{(A)}_{^6\mathrm{He}+\alpha}(D)$ at $D = 4$–5 fm. This is

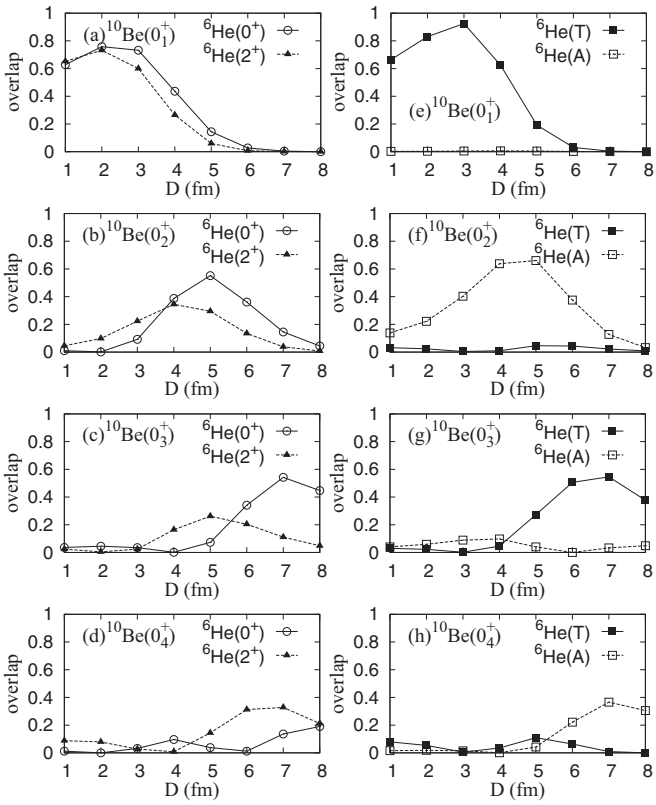

FIG. 8. ^{6}He + α components in ^{10}Be(0^+) obtained by the $D \leqslant 8$ calculation. [(a)–(d)] Squared overlaps of ^{10}Be(0^+) with $\Phi^{[0\otimes 0]_0}_{^6\mathrm{He}+\alpha}(D)$ and $\Phi^{[2\otimes 2]_0}_{^6\mathrm{He}+\alpha}(D)$. [(e)–(h)] Squared overlaps of ^{10}Be(0^+) with $\Phi^{(T)}_{^6\mathrm{He}+\alpha}(D)$ and $\Phi^{(A)}_{^6\mathrm{He}+\alpha}(D)$.

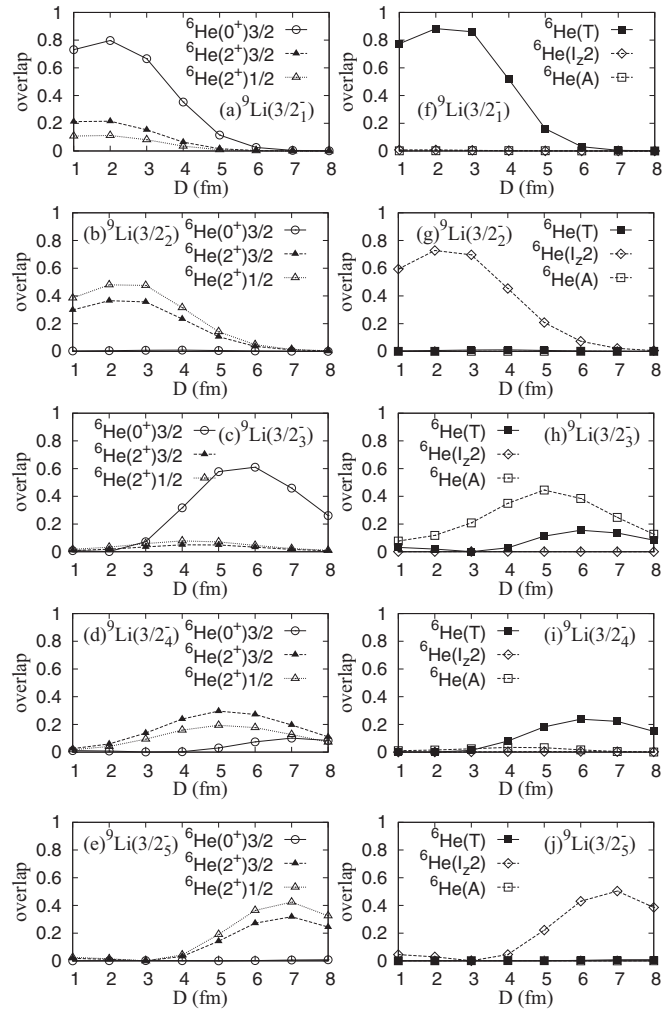

FIG. 9. ^{6}He + t components in ^{9}Li($3/2^-$) obtained by the $D \leqslant 8$ calculation. Panels (a)–(e) show squared overlaps of ^{9}Li($3/2^-$) with $\Phi^{[0\otimes 3/2]_{3/2}}_{^6\mathrm{He}+t}(D)$, $\Phi^{[2\otimes 3/2]_{3/2}}_{^6\mathrm{He}+t}(D)$, and $\Phi^{[2\otimes 1/2]_{3/2}}_{^6\mathrm{He}+t}(D)$. Panels (f)–(j) show squared overlaps of the ^{9}Li($3/2^-$) with $\Phi^{(T)}_{^6\mathrm{He}+t}(D)$, $\Phi^{(A)}_{^6\mathrm{He}+t}(D)$, and $\Phi^{(I_z2)}_{^6\mathrm{He}+t}(D)$.

consistent with the molecular σ-orbital structure of ^{10}Be(0^+_2), as discussed in preceding works. The fact that ^{10}Be(0^+_1) and ^{10}Be(0^+_2) can be clearly classified by the strong-coupling ^{6}He + α wave functions indicates that these states have strong-coupling cluster features rather than weak-coupling ones. In the strong-coupling cluster picture, the excitation from ^{10}Be(0^+_1) to ^{10}Be(0^+_2) is understood as a rotation of the deformed ^{6}He-cluster from the transverse configuration to the aligned configuration with some extent of spatial development of clustering. Because of the difference in the ^{6}He-cluster orientation, i.e., the difference in two-neutron configurations, the ISM transition is suppressed for the transition between ^{10}Be(0^+_1) and ^{10}Be(0^+_2), even though the ^{10}Be(0^+_2) state has the developed cluster structure.

The ^{6}He + α resonance states, ^{10}Be(0^+_3) and ^{10}Be(0^+_4), have spatially developed cluster structures with significant cluster components at D = 6–7 fm. These states show intermediate features between strong- and weak-coupling cluster structures. The ^{10}Be(0^+_3) state has the dominant component $\Phi^{(T)}_{^6\mathrm{He}+\alpha}(D)$ at D = 6–7 fm and is interpreted as a higher nodal state excited from the ground state in the model space of the transverse configuration (f). It has a significant ^{6}He(0^+) + α component with a peak at D = 7 fm and can be regarded as a ^{6}He(0^+) + α resonance. Considering that the peak position of the ^{6}He(0^+) + α component shifts from D = 2–3 fm in the ^{10}Be(0^+_1) state and D = 5 fm in the ^{10}Be(0^+_2) state to D = 7 fm in the ^{10}Be(0^+_3), the ^{10}Be(0^+_2) and ^{10}Be(0^+_3) states can be interpreted as the first and second nodal ^{6}He(0^+) + α states built on the ground state, respectively. ^{10}Be(0^+_4) has a relatively larger ^{6}He(2^+) + α component at D = 6–7 fm and is regarded as a ^{6}He(2^+) + α resonance.

The bound states ^{9}Li($3/2^-_1$) and ^{9}Li($3/2^-_2$) in ^{9}Li can also be clearly classified by the strong-coupling ^{6}He + t wave functions. The ^{9}Li ground state has a dominant overlap with $\Phi^{(T)}_{^6\mathrm{He}+t}(D)$ at D = 2–3 fm and almost no overlap with $\Phi^{(A)}_{^6\mathrm{He}+\alpha}(D)$, which is suppressed by the Pauli blocking effect at short distance. The ^{9}Li($3/2^-_2$) state is dominated by $\Phi^{(I_z2)}_{^6\mathrm{He}+t}(D)$ at $D \sim 2$ fm and can be regarded as the $K = 3/2$ state. The resonance states of ^{9}Li($3/2^-$) have significant cluster components in the D = 5–7 fm region, indicating a spatially developed ^{6}He + t clustering. ^{9}Li($3/2^-_3$) has a significant

^{6}He$(0^+)+t$ component and a relatively small ^{6}He$(2^+)+t$ component and is therefore regarded as a weak-coupling ^{6}He$(0^+)+t$ cluster resonance. The ^{9}Li$(3/2^-_4)$ and ^{9}Li$(3/2^-_5)$ states can be regarded as ^{6}He$(2^+)+t$ cluster resonances because they have significant ^{6}He$(2^+)+t$ components and relatively small ^{6}He$(0^+)+t$ components.

The appearance of the weak-coupling ^{6}He$(0^+)+t$ cluster resonance in ^{9}Li$(3/2^-_3)$ is a specific feature of the ^{9}Li system and differs from the ^{10}Be system, where each ^{6}He$+\alpha$ cluster resonance is not a pure weak-coupling ^{6}He$(I^+)+\alpha$ state. One of the key reasons for this difference between ^{9}Li and ^{10}Be is the presence or absence of the molecular σ-orbital structure below the threshold energy. In ^{10}Be, the molecular σ-orbital structure is favored and appears in ^{10}Be(0^+_2). Note that the molecular σ-orbital structure corresponds to the ^{6}He$(A)+\alpha$ wave function in the present model. It is important that the orthogonal condition of ^{10}Be(0^+_2) to the ground state is satisfied by the orthogonality of the orientation of the deformed ^{6}He cluster. In higher states, the ^{6}He$+\alpha$ clustering develops, maintaining the orthogonal condition to the lower states, ^{10}Be(0^+_1) and ^{10}Be(0^+_2). The existence of ^{10}Be(0^+_2) with the aligned configuration ^{6}He$(A)+\alpha$ at a moderate distance ($D=4$–5 fm) somewhat suppresses the weak-coupling feature of ^{6}He$+\alpha$ cluster resonances because the condition orthogonal to ^{10}Be(0^+_2) depends on the orientation of the deformed ^{6}He cluster. By contrast, the molecular σ-orbital structure is not favored in ^{9}Li due to the asymmetry of the $\alpha+t$ core. In the developed cluster states, the rotational symmetry of the subsystem ^{6}He is restored in the absence of the molecular σ-orbital structure, and the weak-coupling ^{6}He$+t$ clustering is favored to form the ^{6}He$(0^+)+t$ cluster resonance in ^{9}Li$(3/2^-_3)$.

B. Isoscalar monopole excitation and its relation to strong-coupling cluster structures

The enhancement of ISM transitions to cluster states in stable and unstable nuclei has been discussed [26,62–64]. As discussed by Yamada *et al.*, ISM strengths are enhanced for transitions from the ground state to cluster excited states because the ISM operator $\mathcal{M}(IS0)$ excites intercluster motion through the r^2 term in $\mathcal{M}(IS0)$ [64]. As shown in Ref. [64], $\mathcal{M}(IS0)$ can be rewritten as

$$\mathcal{M}(IS0)=\frac{A_1A_2}{A}r^2+\sum_{i\in C}(\boldsymbol{r}_i-\boldsymbol{R}_1)^2+\sum_{i\in C'}(\boldsymbol{r}_i-\boldsymbol{R}_2)^2, \tag{20}$$

where $\boldsymbol{R}_1$ and $\boldsymbol{R}_2$ are the center-of-mass coordinates of the first (C) and second (C') clusters, respectively. If antisymmetrization is ignored, then the first term excites the intercluster motion while the second and third terms cause the ISM excitations of C and C' clusters.

In ISM excitations, the $\mathcal{M}(IS0)$ operated state, $\mathcal{M}(IS0)|\text{g.s.}\rangle$, is regarded as the doorway state that is initially produced by ISM excitation. Provided that excitations of the intercluster motion (cluster mode) are well decoupled from the internal excitations of the clusters, the ISM strengths of cluster states are simply distributions of the doorway state $\mathcal{M}(IS0)|\text{g.s.}\rangle$ projected onto the cluster model space, $\hat{P}(C+C')\mathcal{M}(IS0)|\text{g.s.}\rangle$, which approximately corresponds to the doorway state excited from the ground state by the r^2 operator. Here $\hat{P}(C+C')$ is the projection operator onto the $C+C'$ cluster model space. In the present case, the ISM strengths indicate the distributions of the projected doorway state $\hat{P}(^6\text{He}+\alpha(t))\mathcal{M}(IS0)|\text{g.s.}\rangle$ in the ^{6}He$+\alpha(t)$ cluster model space.

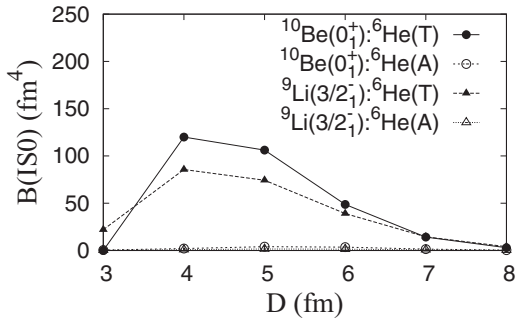

FIG. 10. ISM strengths $B(IS0;\text{g.s.}\to\Phi^{(T,A)}_{^6\text{He}+\alpha(t)}(D))$ for the transitions from the ^{10}Be and ^{9}Li ground states obtained by the $D\leqslant 8$ calculation to $\Phi^{(T,A)}_{^6\text{He}+\alpha(t)}(D)$. $B(IS0;\text{g.s.}\to\Phi^{(T,A)}_{^6\text{He}+\alpha(t)}(D))$ is defined in Eq. (21).

As discussed previously, the low-lying states of ^{10}Be and ^{9}Li can be understood to be strong-coupling cluster structures. In particular, the ground state is dominated by the transverse configuration $\Phi^{(T)}_{^6\text{He}+\alpha(t)}(D)$ at a distance $D=2$–3 fm. Therefore, the projected doorway state $P(^6\text{He}+\alpha(t))\mathcal{M}(IS0)|\text{g.s.}\rangle$ is approximately included by the subspace with a specific configuration $\Phi^{(T)}_{^6\text{He}+\alpha(t)}(D)$ because the ISM operator excites the intercluster motion through the r^2 term but does not change the orientation of the deformed ^{6}He cluster. Figure 10 shows the ISM strengths for transition from the ^{10}Be and ^{9}Li ground state to specific configurations, namely, the transverse configuration $\Phi^{(T)}_{^6\text{He}+\alpha(t)}(D)$ and the aligned configuration $\Phi^{(A)}_{^6\text{He}+\alpha(t)}(D)$. The strengths of the ISM transitions from the ground state are calculated as

$$B\left(IS0;\text{g.s.}\to\Phi^{(T,A)}_{^6\text{He}+\alpha(t)}(D)\right)=\frac{1}{2J+1}\left|\langle\text{g.s.}||\mathcal{M}(IS0)|\right|\Lambda_{\text{g.s.}}\Phi^{(T,A)}_{^6\text{He}+\alpha(t)}(D)\rangle\Big|^2, \tag{21}$$

$$\Lambda_{\text{g.s.}}\equiv 1-|\text{g.s.}\rangle\langle\text{g.s.}|, \tag{22}$$

where the normalizations of the initial and final states are chosen to be one and the orthogonal condition of the final state to the initial state is satisfied by the projection operator $\Lambda_{\text{g.s.}}$. As seen in the figure, the calculated ISM strengths show significant transitions to $\Phi^{(T)}_{^6\text{He}+\alpha(t)}(D)$ at $D=4$–5 fm but almost no transition to $\Phi^{(A)}_{^6\text{He}+\alpha(t)}(D)$, as would be expected from the dominance of the $\Phi^{(T)}_{^6\text{He}+\alpha(t)}(D)$ component in the initial state $|\text{g.s.}\rangle$. This means that the doorway state excited from the ground state by the ISM operator dominantly contains the transverse configuration of the ^{6}He cluster.

Let us go back to the IMS strengths obtained by the three calculations, (c+f), $D\leqslant 8$, and $D\leqslant 15$. As shown in Table II,

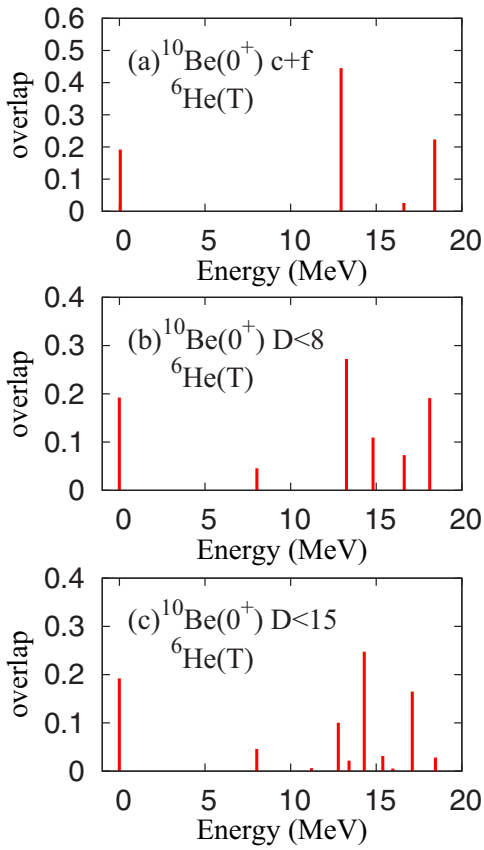

FIG. 11. Distributions of squared overlaps of $\Phi^{(T)}_{^6\mathrm{He}+\alpha}(D)$ at $D =$ 5 fm for the ^{10}Be(0^+) obtained by the (c+f), $D \leqslant 8$, and $D \leqslant 15$ calculations.

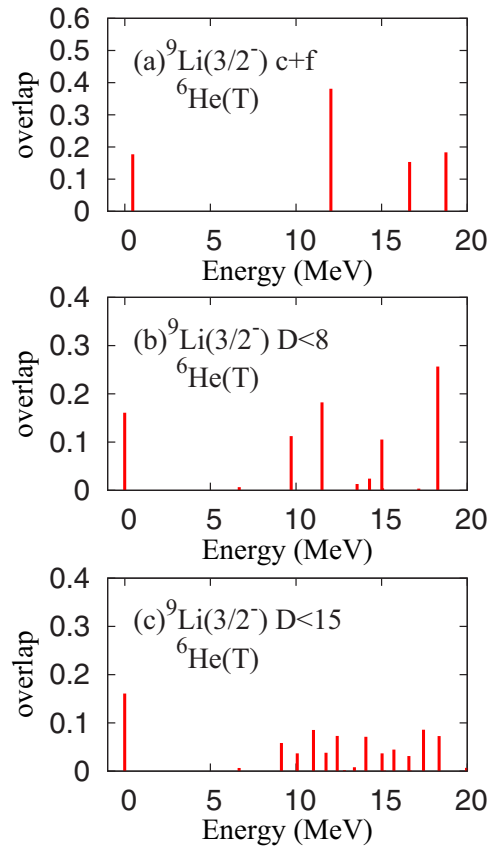

FIG. 12. Distributions of squared overlaps of $\Phi^{(T)}_{^6\mathrm{He}+t}(D)$ at $D =$ 5 fm for the ^{9}Li($3/2^-$) obtained by the (c+f), $D \leqslant 8$, and $D \leqslant 15$ calculations.

the EWS obtained by the (c+f) calculation is almost consistent with that obtained by the $D \leqslant 8$ calculation with full ^{6}He configurations. This indicates that the doorway state directly produced from the ground state by the ISM operator are mostly contained in the truncated model space of configurations (c) and (f). As shown in Figs. 5(a) and 6(a), the ISM strengths are concentrated in a few low-lying states in the (c+f) calculation, meaning that the doorway state is distributed in these few states of the truncated model space. However, in the $D \leqslant 8$ calculation of the full configurations of $^6\mathrm{He} + \alpha(t)$, the ISM strengths are somewhat fragmented through the coupling of the configuration $\Phi^{(T)}_{^6\mathrm{He}+\alpha(t)}(D)$ with other configurations. The ISM strengths should reflect the distributions of the $\Phi^{(T)}_{^6\mathrm{He}+\alpha}(D)$ and $\Phi^{(T)}_{^6\mathrm{He}+t}(D)$ components in the resulting ^{10}Be(0^+) and ^{9}Li($3/2^-$). As already shown in Fig. 10, the $\Phi^{(T)}_{^6\mathrm{He}+\alpha(t)}(D)$ configuration has a strong ISM transition in the $D = 4$–5 fm region, meaning that the doorway state excited from the ground state by the ISM operator has a large overlap with this state. Figures 11 and 12 show distributions of the squared overlaps of ^{10}Be(0^+) and ^{9}Li($3/2^-$) obtained by the three calculations for $\Phi^{(T)}_{^6\mathrm{He}+\alpha}(D)$ and $\Phi^{(T)}_{^6\mathrm{He}+t}(D)$ at $D = 5$ fm. Comparing the results of Figs. 5 and 6 with those of Figs. 11 and 12, the ISM strength distributions can be qualitatively described by the distributions of the $\Phi^{(T)}_{^6\mathrm{He}+\alpha(t)}(D)$ component. In the $D \leqslant 8$ and $D \leqslant 15$ calculations of ^{9}Li, the fragmentation of the $\Phi^{(T)}_{^6\mathrm{He}+t}(D)$ component due to coupling with other configurations describes the strong fragmentation of the ISM strengths for the $^6\mathrm{He} + t$ cluster resonances at 10–15 MeV. Compared with ^{9}Li, the fragmentation of the $\Phi^{(T)}_{^6\mathrm{He}+\alpha}(D)$ component is relatively weaker in the $D \leqslant 8$ and $D \leqslant 15$ calculations of ^{10}Be, and significant components remain in the $E_x = 13$–15 MeV region for the ^{10}Be(0^+_3) and ^{10}Be(0^+_4) states.

Let us move to a general discussion of the doorway state that is excited from the ground state to the cluster states by the ISM operator. As mentioned previously, the projected doorway state approximately corresponds to the r^2 operated state of the ground state. In case where the ground state contains a deformed cluster with a specific orientation, inter-cluster motion is excited from the ground state to the doorway state with the orientation of the cluster maintained as it is in the ground state, because the r^2 operator does not induce rotation in clusters. Schematic illustrations of this are shown in Fig. 13. When the system consists of two spinless clusters such as $^{16}\mathrm{O} + \alpha$, in which both clusters are ls-closed shell nuclei, the projected doorway state can be concentrated on a $^{16}\mathrm{O} + \alpha$ cluster state, and, therefore, the ISM transition should be strong for the $^{16}\mathrm{O} + \alpha$ cluster state [Fig. 13(a)]. However, in the cases of $^6\mathrm{He} + \alpha$ and $^6\mathrm{He} + t$ cluster states in ^{10}Be and ^{9}Li, the

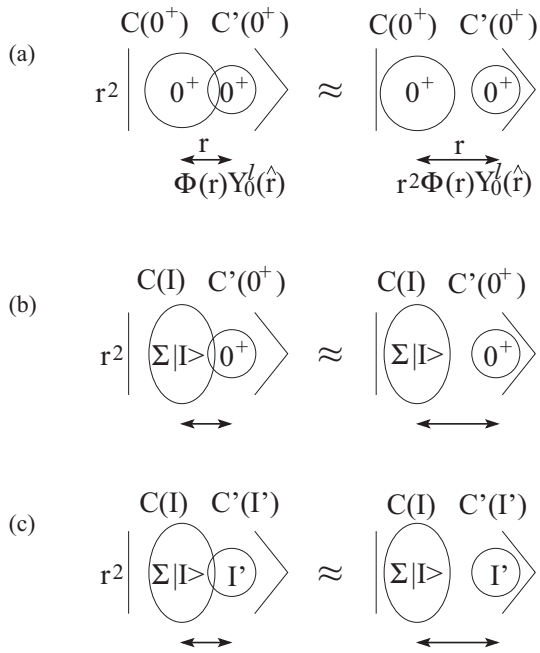

FIG. 13. Schematics of ISM excitations to cluster states. (a) A system of two clusters that are spinless ls-closed shell nuclei. (b) A system consisting of a deformed cluster and a spinless ls-closed cluster. (b) A system consisting of a deformed cluster and a finite-spin cluster.

^{6}He cluster is not an ls-closed shell nucleus but is deformed in the ^{10}Be and ^{9}Li ground states due to the Pauli blocking effect between clusters [Figs. 13(b) and 13(c)]. The deformed ^{6}He cluster is a mixed state of different spin states of ^{6}He(I). In the asymptotic region at a large intercluster distance, the deformed cluster is not favored but the angular-momentum eigenstates ^{6}He(I) are favored because of the restoration of the rotational symmetry of the subsystem. Moreover, in the ^{6}He + t system, the second cluster (t) has a finite intrinsic spin $I' = 1/2$. Therefore, the projected doorway state is fragmented in ^{6}He + t cluster states through the coupling of the angular momenta (I and I') of the clusters and the orbital angular momentum of the intercluster motion. As a result, the ISM strengths can be strongly fragmented. In the ^{6}He + α system, because the angular-momentum coupling is not so strong for the spinless α cluster, the fragmentation of the doorway state can be weaker than that in the ^{6}He + t system. Therefore, the fragmentation of the ISM strengths to ^{6}He + α cluster states is not as strong as that to ^{6}He + t cluster states.

C. Weak-coupling cluster resonances

As discussed previously, the cluster resonances ^{10}Be(0^+_3), ^{10}Be(0^+_4), ^{9}Li($3/2^-_3$), and ^{9}Li($3/2^-_{4,5}$) have significant weak-coupling cluster components of ^{6}He(0^+) + α, ^{6}He(2^+) + α, ^{6}He(0^+) + t, and ^{6}He(2^+) + t, respectively, in the long-distance region (D = 6–7 fm). Therefore, the weak-coupling cluster components can serve as more direct probes for cluster resonances than the ISM strengths, which reflect the strong-coupling cluster component of the $\Phi^{(T)}_{^6\mathrm{He}+\alpha(t)}$.

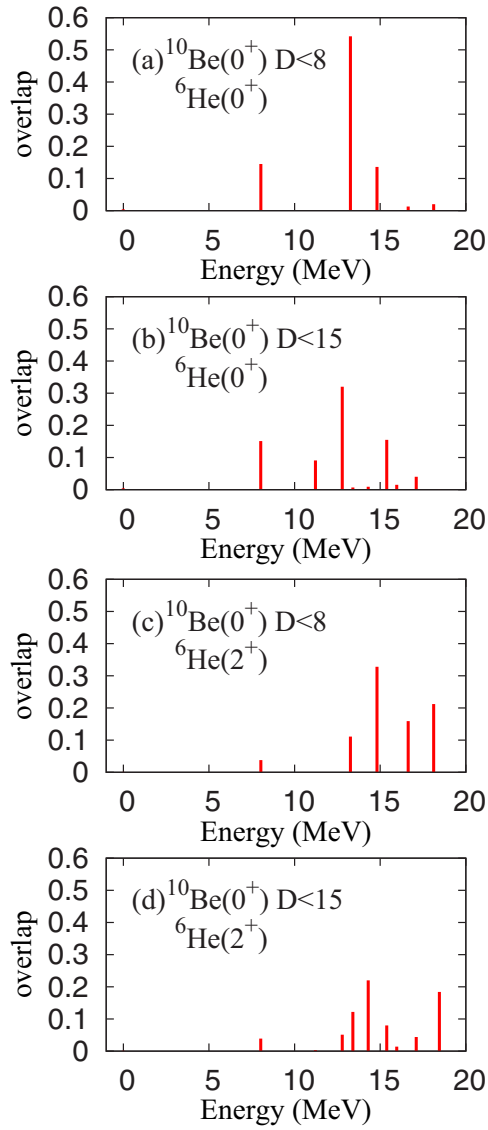

FIG. 14. Distributions of ^{6}He(0^+) + α and ^{6}He(2^+) + α components in ^{10}Be(0^+). [(a) and (c)] Squared overlaps of ^{10}Be(0^+) obtained by the $D \leqslant 8$ calculation with $\Phi^{[0\otimes 0]_0}_{^6\mathrm{He}+\alpha}(D)$ and $\Phi^{[2\otimes 2]_0}_{^6\mathrm{He}+\alpha}(D)$ at D = 7 fm. [(b) and (d)] Same but for the $D \leqslant 15$ calculation.

Distribution of ^{6}He(0^+) + α and ^{6}He(2^+) + α components at D = 7 fm in ^{10}Be are shown in Fig. 14. The figure shows the squared overlaps of $\Phi^{[I\otimes J']_J}_{^6\mathrm{He}+\alpha}(D)$ with the ^{10}Be(0^+) state obtained using the $D \leqslant 8$ and $D \leqslant 15$ calculations. In the $D \leqslant 8$ calculation, the ^{6}He(0^+) + α component is concentrated on the ^{10}Be(0^+_3) state at 13 MeV, whereas the ^{6}He(2^+) + α component is significant in the ^{10}Be(0^+_4) state at 15 MeV [Figs. 14(a) and 14(c)]. In the $D \leqslant 15$ calculation, the concentration of the ^{6}He(0^+) + α component around 13 MeV and that of the ^{6}He(2^+) + α component around 15 MeV can be seen, although the components are somewhat fragmented [Figs. 14(b) and 14(d)].

Figure 15 shows the distribution of the ^{6}He(0^+) + t and ^{6}He(2^+) + t components at D = 7 fm in ^{9}Li. In the $D \leqslant 8$ calculation, the ^{6}He(0^+) + t component is concentrated at

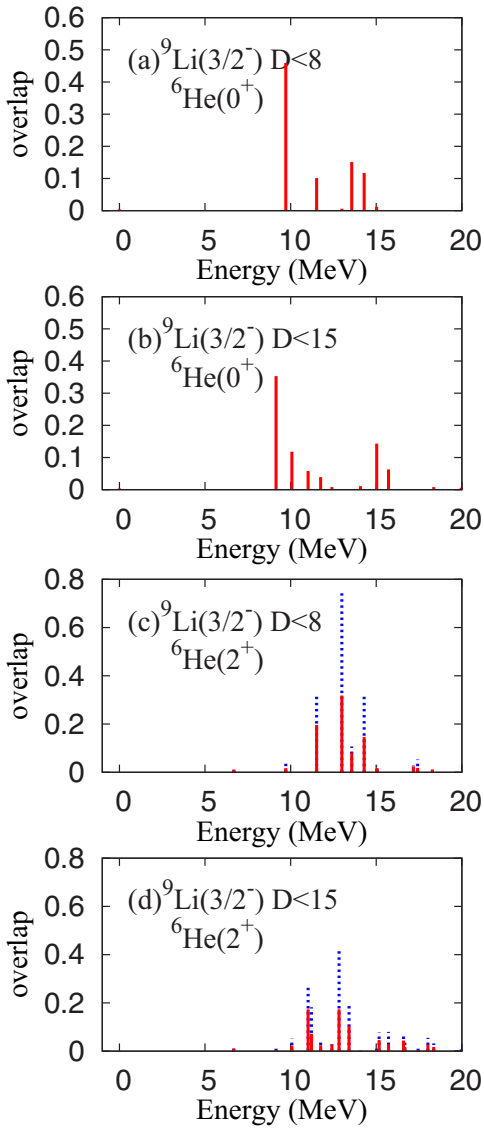

FIG. 15. Distributions of ^{6}He(0$^+$) + t and ^{6}He(2$^+$) + t components in ^{9}Li(3/2$^-$). [(a) and (c)] Squared overlaps of ^{9}Li(3/2$^-$) obtained by the $D \leqslant 8$ calculation with $\Phi^{[0\otimes 3/2]_{3/2}}_{^6\mathrm{He}+t}(D)$ (solid lines), $\Phi^{[2\otimes 3/2]_{3/2}}_{^6\mathrm{He}+t}(D)$ (solid lines), and $\Phi^{[2\otimes 1/2]_{3/2}}_{^6\mathrm{He}+t}(D)$ (dashed lines) at $D =$ 7 fm. [(b) and (d)] Same overlaps for the $D \leqslant 15$ calculation.

10 MeV for the ^{9}Li(3/2$^-_3$) state [Fig. 15(a)]. Even in the $D \leqslant 15$ calculation, the significant ^{6}He(0$^+$) + t component is found in the corresponding energy region around 9 MeV [Figs. 15(b)], whereas the ^{6}He(2$^+$) + t components are significant in the 11- to 14-MeV region [Figs. 15(d)].

Note that the distributions of the ^{6}He(0$^+$) + α and ^{6}He(0$^+$) + t components shown in Figs. 14 and 15 are not consistent with the ISM strength distributions shown in Figs. 5 and 6. In particular, despite the significant ^{6}He(0$^+$) + t component in the ^{9}Li(3/2$^-$) state around 10 MeV, there is no significant ISM strength in the corresponding energy region. Thus, there is no one-to-one correspondence between the ISM excitation and the ^{6}He(0$^+$) + α component, because the ISM operator more directly excites the specific type of strong-coupling cluster structures embedded in the ground state.

As seen in Figs. 14 and 15, the distribution of ^{6}He(0$^+$) + α, ^{6}He(2$^+$) + α, ^{6}He(0$^+$) + t, and ^{6}He(2$^+$) + t components show enhanced peaks around 12–13 MeV for ^{10}Be(0$^+_3$), 14–15 MeV for ^{10}Be(0$^+_4$), 9–10 MeV for ^{9}Li(3/2$^-_3$), and 11–14 MeV for ^{9}Li(3/2$^-_{4,5}$). Therefore, resonant elastic and inelastic scatterings can be better experimental probes than ISM strengths for identifying each cluster resonance.

V. SUMMARY

The ISM transitions from the ground to the cluster states in ^{10}Be and ^{9}Li were investigated using the ^{6}He + α and ^{6}He + t cluster models, respectively. In the calculation, the resonance states were obtained in a bound-state approximation. The ^{6}He + α and ^{6}He + t widths of the resonances were estimated by using the reduced-width amplitudes obtained from the calculation for $D \leqslant 8$ fm. The coupling with continuum states evaluated by changing the boundary size from $D \leqslant 8$ fm to $D \leqslant 15$ fm showed consistent results with the decay widths estimated by the bound-state approximation for $D \leqslant 8$ fm.

In ^{10}Be, ^{6}He + α cluster resonances were obtained as the ^{10}Be(0$^+_3$) and ^{10}Be(0$^+_4$) states above the ^{6}He + α threshold energy. The significant ISM strengths were obtained for transitions to these resonances. In ^{9}Li, the ^{6}He + t cluster resonances were obtained as the ^{9}Li(3/2$^-_{3,4,5}$) state above the ^{6}He + t threshold energy. Unlike the ^{6}He + α cluster resonances in ^{10}Be, the ISM strengths are strongly fragmented and show no enhancement for these ^{6}He + t cluster resonances.

By analyzing the cluster components of excited states, the relation of the ISM excitations to the cluster components were discussed. It was found that the ISM strength distributions do not directly correspond to the distributions of the ^{6}He(0$^+$) + α and ^{6}He(0$^+$) + t components but are distributed via components of the deformed ^{6}He cluster configuration with a specific orientation. The ISM strengths of cluster states are the distributions of the doorway state in the cluster model space, which is excited from the ground state by the r^2 operator. Because the ^{10}Be and ^{9}Li ground states are dominated by the transverse configuration of the deformed ^{6}He cluster, the doorway state also dominantly contains the transverse configuration, as the ISM operator excites the intercluster motion through the r^2 term but does not change the orientation of the deformed ^{6}He cluster. The doorway state distributions, which are originally concentrated on the specific configuration, are fragmented in final states in the full model space due to mixing with other configurations and angular-momentum coupling. The above is an interpretation of the fragmentation of the ISM strengths in ^{10}Be and ^{9}Li. Note that the ISM excitations more directly reflect the strong-coupling cluster features that are originally embedded in the ground state rather than the weak-coupling cluster features. In other words, the ISM strengths can be a good probe for cluster states provided that they contain the strong-coupling cluster component that is directly excited by the monopole operator from the ground state. For weak-coupling cluster resonances having weak ISM strengths, resonant elastic and inelastic

scatterings can be alternative probes for identifying the cluster states.

ACKNOWLEDGMENTS

The author thanks Dr. Kimura and Dr. Suhara for fruitful discussions. The computational calculations of this work were performed using the supercomputer in the Yukawa Institute for theoretical physics, Kyoto University. This work was supported by JSPS KAKENHI Grant No. 26400270.

APPENDIX: CALCULATION OF PARTIAL DECAY WIDTHS IN THE BOUND STATE APPROXIMATION

In the default $D \leqslant 8$ calculation, the resonance states are obtained as bound-state solutions in the model space of $D \leqslant 8$ fm. In a bound-state approximation, the partial decay width $\Gamma_{I\otimes J'}$ of a resonance state for $^6\mathrm{He}(I^+) + \alpha(t)$ channels with angular-momentum coupling $[I \otimes J']_J$ can be estimated from the reduced width amplitude $y(a)$ of the corresponding channel at a channel radius a,

$$\Gamma_{I\otimes J'} = \frac{2ka}{F_l^2(ka) + G_l^2(ka)}\gamma^2(a), \tag{A1}$$

$$\gamma^2(a) = \frac{\hbar^2}{2\mu a}[ay(a)]^2, \tag{A2}$$

where F_l and G_l are the regular and irregular Coulomb functions, respectively; k is the momentum of intercluster motion in the asymptotic region; μ is the reduced mass; $\gamma^2(a)$ is the so-called reduced width; and l is the orbital angular momentum of the relative motion. In the present work, $y(a)$ is approximately calculated using the overlap with the $^6\mathrm{He}(I^+) + \alpha(t)$ cluster wave function $\Phi^{[I\otimes J']_J}_{^6\mathrm{He}+\alpha(t)}(D = a)$ by means of the method proposed in Ref. [65] as

$$ay(a) \approx \frac{1}{\sqrt{2}}\left(\frac{2\gamma}{\pi}\right)^{1/4}\left\langle \Psi^{J^\pi_k} \middle| \Phi^{[I\otimes J']_J}_{^6\mathrm{He}+\alpha(t)}(D = a)\right\rangle. \tag{A3}$$

[1] W. von Oertzen, M. Freer, and Y. Kanada-En'yo, Phys. Rep. **432**, 43 (2006).
[2] Y. Kanada-En'yo and H. Horiuchi, Prog. Theor. Phys. Suppl. **142**, 205 (2001).
[3] Y. Kanada-En'yo, M. Kimura, and A. Ono, Prog. Theor. Exp. Phys. **2012**, 01A202 (2012).
[4] M. Ito and K. Ikeda, Rep. Prog. Phys. **77**, 096301 (2014).
[5] S. Okabe, Y. Abe, and H. Tanaka, Prog. Theor. Phys. **57**, 866 (1977); S. Okabe and Y. Abe, *ibid.* **59**, 315 (1978); **61**, 1049 (1979).
[6] M. Seya, M. Kohno, and S. Nagata, Prog. Theor. Phys. **65**, 204 (1981).
[7] W. von Oertzen, Z. Phys. A **354**, 37 (1996); **357**, 355 (1997).
[8] W. von Oertzen, Nuovo Cimento **110**, 895 (1997).
[9] K. Arai, Y. Ogawa, Y. Suzuki, and K. Varga, Phys. Rev. C **54**, 132 (1996).
[10] A. Dote, H. Horiuchi, and Y. Kanada-En'yo, Phys. Rev. C **56**, 1844 (1997).
[11] Y. Ogawa, K. Arai, Y. Suzuki, and K. Varga, Nucl. Phys. A **673**, 122 (2000).
[12] Y. Kanada-En'yo, H. Horiuchi, and A. Dote, Phys. Rev. C **60**, 064304 (1999).
[13] N. Itagaki and S. Okabe, Phys. Rev. C **61**, 044306 (2000).
[14] N. Itagaki, S. Okabe, and K. Ikeda, Phys. Rev. C **62**, 034301 (2000).
[15] N. Itagaki, S. Hirose, T. Otsuka, S. Okabe, and K. Ikeda, Phys. Rev. C **65**, 044302 (2002).
[16] P. Descouvemont and D. Baye, Phys. Lett. B **505**, 71 (2001).
[17] P. Descouvemont, Nucl. Phys. A **699**, 463 (2002).
[18] Y. Kanada-En'yo and H. Horiuchi, Phys. Rev. C **66**, 024305 (2002).
[19] Y. Kanada-En'yo and H. Horiuchi, Phys. Rev. C **68**, 014319 (2003).
[20] M. Ito, K. Kato, and K. Ikeda, Phys. Lett. B **588**, 43 (2004).
[21] W. von Oertzen and H. G. Bohlen, C. R. Physique **4**, 465 (2003).
[22] K. Arai, Phys. Rev. C **69**, 014309 (2004).
[23] M. Ito, Phys. Lett. B **636**, 293 (2006).
[24] M. Ito, N. Itagaki, H. Sakurai, and K. Ikeda, Phys. Rev. Lett. **100**, 182502 (2008).
[25] M. Dufour, P. Descouvemont, and D. Baye, Nuc. Phys. A **836**, 242 (2010).
[26] M. Ito, Phys. Rev. C **83**, 044319 (2011).
[27] M. Ito, N. Itagaki, and K. Ikeda, Phys. Rev. C **85**, 014302 (2012).
[28] Y. Kanada-En'yo, Phys. Rev. C **85**, 044320 (2012).
[29] K. Fujimura, D. Baye, P. Descouvemont, Y. Suzuki, and K. Varga, Phys. Rev. C **59**, 817 (1999).
[30] Y. Kanada-En'yo, Phys. Rev. C **66**, 011303 (2002).
[31] S. Hamada, M. Yasue, S. Kubono, M. H. Tanaka, and R. J. Peterson, Phys. Rev. C **49**, 3192 (1994).
[32] N. Soic *et al.*, Europhys. Lett. **34**, 7 (1996).
[33] N. Curtis, D. D. Caussyn, N. R. Fletcher, F. Marechal, N. Fay, and D. Robson, Phys. Rev. C **64**, 044604 (2001).
[34] J. A. Liendo, N. Curtis, D. D. Caussyn, N. R. Fletcher, and T. Kurtukian-Nieto, Phys. Rev. C **65**, 034317 (2002).
[35] N. R. Fletcher, D. D. Caussyn, F. Marechal, N. Curtis, and J. A. Liendo, Phys. Rev. C **68**, 024316 (2003).
[36] N. Curtis *et al.*, Phys. Rev. C **70**, 014305 (2004).
[37] S. Ahmed *et al.*, Phys. Rev. C **69**, 024303 (2004).
[38] M. Milin *et al.*, Nucl. Phys. A **753**, 263 (2005).
[39] M. Freer *et al.*, Phys. Rev. Lett. **96**, 042501 (2006).
[40] H. G. Bohlen, T. Dorsch, T. Kokalova, W. von Oertzen, C. Schulz, and C. Wheldon, Phys. Rev. C **75**, 054604 (2007).
[41] N. Curtis, N. I. Ashwood, M. Freer, T. Munoz-Britton, C. Wheldon, V. A. Ziman, S. Brown, W. N. Catford *et al.*, J. Phys. G **36**, 015108 (2009).
[42] D. Suzuki *et al.*, Phys. Rev. C **87**, 054301 (2013).
[43] H. G. Bohlen *et al.*, Nouvo Cimento A **111**, 841 (1998).
[44] H. G. Bohlen *et al.*, Phys. At. Nucl. **65**, 603 (2002).
[45] A. A. Korsheninnikov *et al.*, Phys. Lett. B **343**, 53 (1995).
[46] M. Freer *et al.*, Phys. Rev. Lett. **82**, 1383 (1999).
[47] M. Freer *et al.*, Phys. Rev. C **63**, 034301 (2001); **64**, 019904 (2001).
[48] A. Saito *et al.*, Nucl. Phys. A **738**, 337 (2004); A. Saito, S. Shimoura, T. Minemura, Y. U. Matsuyama, H. Baba, N. Aoi, T. Gomi, Y. Higurashi *et al.*, Mod. Phys. Lett. A **25**, 1858 (2010).
[49] Z. H. Yang *et al.*, Phys. Rev. Lett. **112**, 162501 (2014).

[50] F. Kobayashi and Y. Kanada-En'yo, Phys. Rev. C **86**, 064303 (2012).
[51] A. N. Kuchera *et al.*, Phys. Rev. C **84**, 054615 (2011); **85**, 069902 (2012); **88**, 039901 (2013).
[52] Y. Kanada-En'yo and T. Suhara, Phys. Rev. C **85**, 024303 (2012).
[53] D. L. Hill and J. A. Wheeler, Phys. Rev. **89**, 1102 (1953); J. J. Griffin and J. A. Wheeler, *ibid.* **108**, 311 (1957).
[54] D. M. Brink, in *Proceedings of the International School of Physics: Enrico Fermi, Course 36*, edited by C. Bloch (Academic Press, New York, 1966).
[55] Y. Kanada-En'yo, H. Horiuchi, and A. Ono, Phys. Rev. C **52**, 628 (1995).
[56] A. B. Volkov, Nucl. Phys. **74**, 33 (1965).
[57] N. Yamaguchi, T. Kasahara, S. Nagata, and Y. Akaishi, Prog. Theor. Phys. **62**, 1018 (1979); R. Tamagaki, *ibid.* **39**, 91 (1968).
[58] T. Suhara and Y. Kanada-En'yo, Prog. Theor. Phys. **123**, 303 (2010).
[59] W. Nortershauser, D. Tiedemann, M. Zakova, Z. Andjelkovic, K. Blaum, M. L. Bissell, R. Cazan, G. W. F. Drake *et al.*, Phys. Rev. Lett. **102**, 062503 (2009).
[60] G. Ewald *et al.*, Phys. Rev. Lett. **93**, 113002 (2004).
[61] A. Ozawa, T. Suzuki, and I. Tanihata, Nucl. Phys. A **693**, 32 (2001).
[62] Y. Suzuki and S. Hara, Phys. Rev. C **39**, 658 (1989).
[63] T. Kawabata *et al.*, Phys. Lett. B **646**, 6 (2007).
[64] T. Yamada, Y. Funaki, T. Myo, H. Horiuchi, K. Ikeda, G. Ropke, P. Schuck, and A. Tohsaki, Phys. Rev. C **85**, 034315 (2012).
[65] Y. Kanada-En'yo, T. Suhara, and Y. Taniguchi, Prog. Theor. Exp. Phys. **2014**, 073D02 (2014).